

## S8 Time Series Analysis

**Ed Cohen**

Room: 536 Huxley

email: [e.cohen@imperial.ac.uk](mailto:e.cohen@imperial.ac.uk)

Use Blackboard to obtain all course resources

Department of Mathematics

Imperial College London

180 Queen's Gate, London SW7 2BZ

With thanks to Prof Andrew Walden

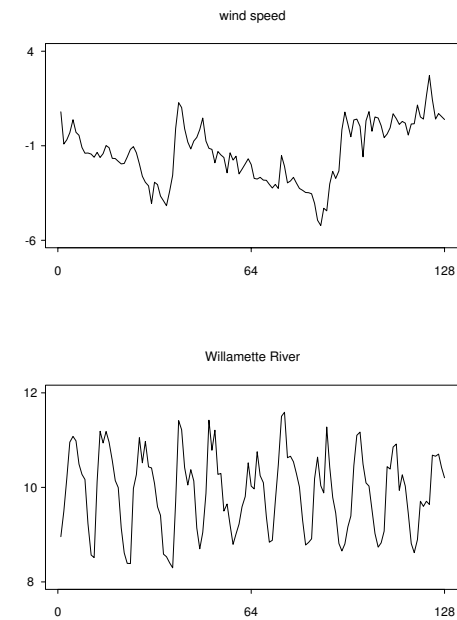


Figure 1: Plots of portions of the first two time series. For both time series the vertical axis is the value of the time series (in unspecified units), while the horizontal axis is time (measured at 0.025 second intervals for the wind speed series and in months for the Willamette River series).

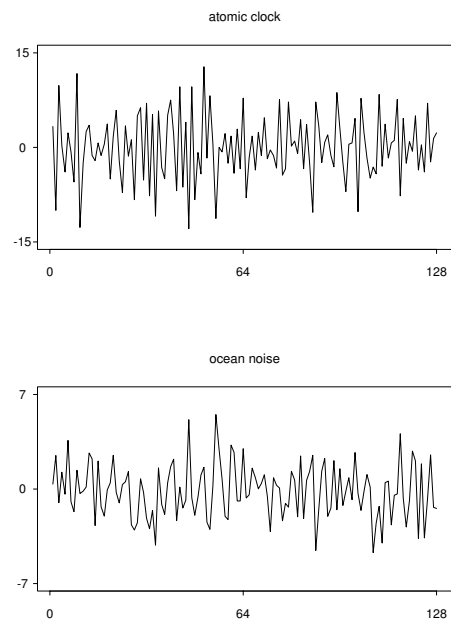


Figure 2: Plots of portions of the next two time series. The horizontal axes are again time (measured in days for the atomic clock series and in seconds for the ocean noise series).

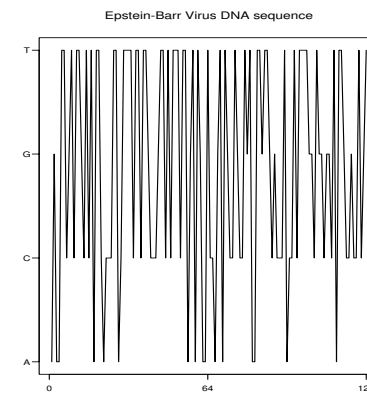


Figure 3: Plot of a portion of the epstein-Barr Virus DNA sequence, made up of the four different bases (bp), thymine (**T**), cytosine (**C**), adenine (**A**) and guanine (**G**). The full EBV DNA sequence consists of approximately 172,000 bp.

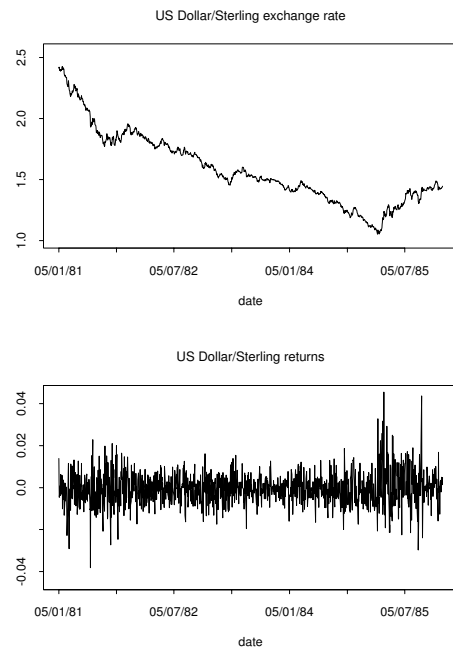


Figure 4: Plots of the US Dollar/Sterling exchange rate from 05/01/81 to 31/12/85 and the associated returns. The horizontal axes are again time (measured in days).

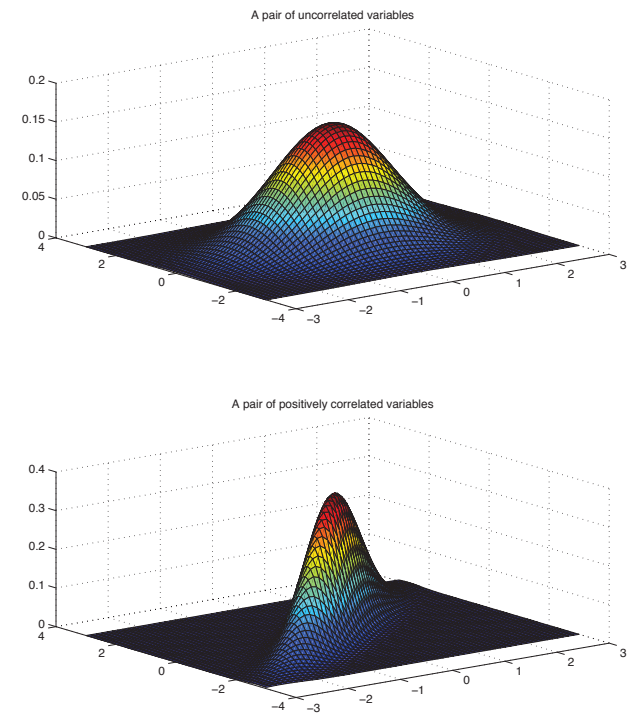


Figure 4a: Bivariate pdfs for two random variables which are uncorrelated (top) or positively correlated (bottom). Bivariate normal distribution used.

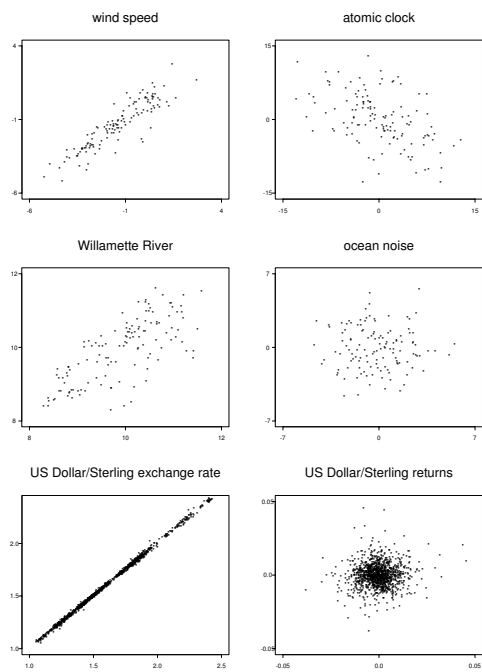


Figure 5: Lag 1 scatter plots for the time series in Figures 1, 2, and 4. In each of these plots, the values of the times series at time  $t + 1$  is plotted on the vertical axis versus the value at time  $t$  on the horizontal axis.

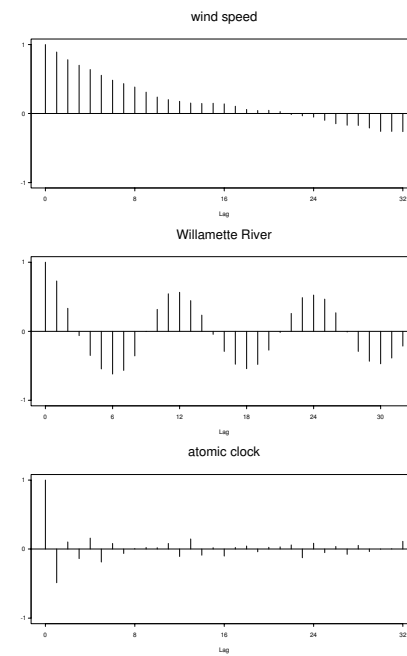


Figure 6: Sample autocorrelations for the time series.

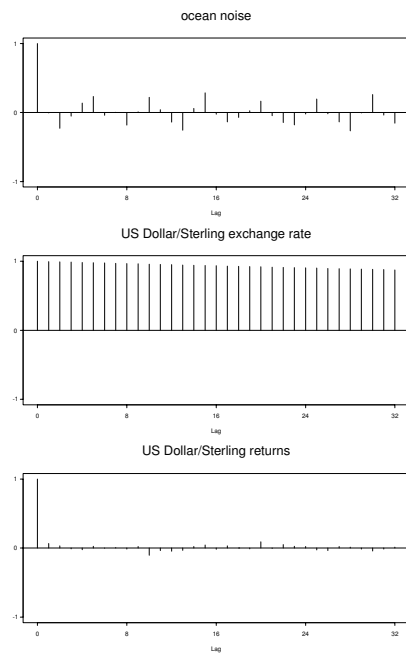


Figure 7: Sample autocorrelations for the time series.

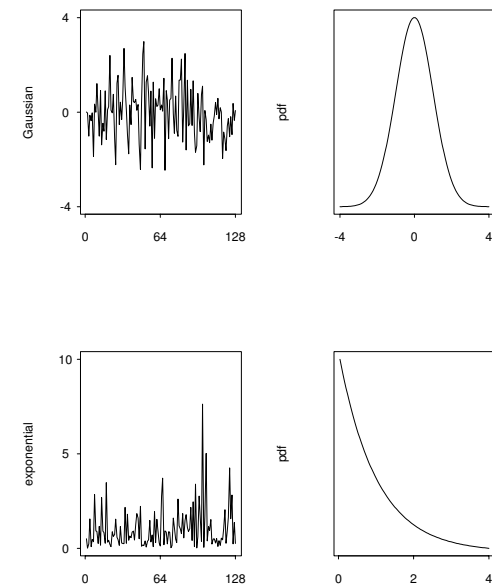


Figure 8: Realizations of two white noise processes and their underlying densities. The distribution for the process in the top left plot is Gaussian (with mean zero and variance 1), while the one for the bottom left plot is Chi-squared with two degrees of freedom (exponential) – this distribution is one-sided (i.e., an rv with this distribution can assume only nonnegative values) and has a heavier tail than the Gaussian distribution. This gives the time series the appearance of having outliers.

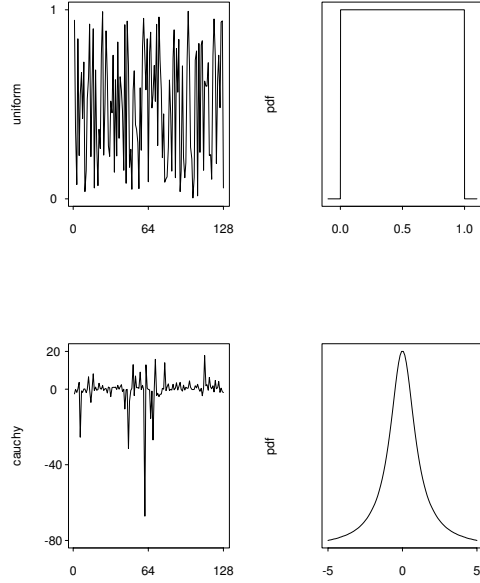


Figure 9: Realizations of two more white noise processes and their underlying densities. The distribution for the process in the top left plot is uniform on the interval  $[0, 1]$ , while the one for the bottom left plot has a Cauchy distribution that has been truncated at  $\pm 10^{10}$  to produce a distribution with finite mean and variance – a requirement for second-order stationarity. The tails for the truncated Cauchy distribution are heavier than for both distributions in Figure 8, while the tails for the uniform distribution are lighter.

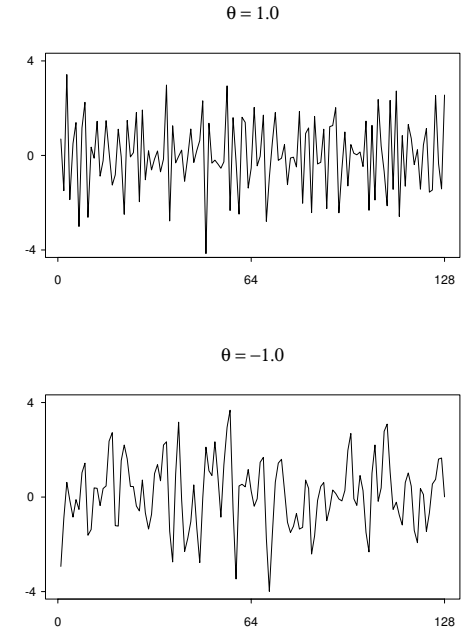


Figure 10: Realizations of size 128 of two first-order Gaussian moving average processes. The top and bottom plots are for processes with  $\theta = 1.0$  and  $\theta = -1.0$  respectively, and  $\sigma_\epsilon^2 = 1.0$  in both cases.

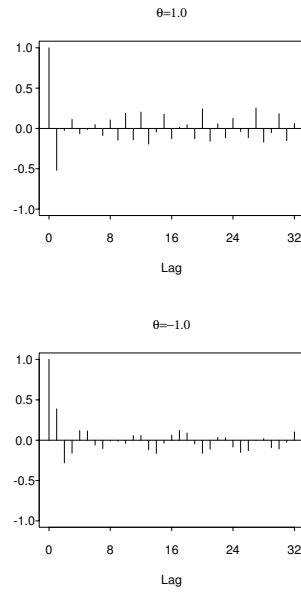


Figure 11: Sample acs for the MA(1) processes shown in Figure 10.

Theoretical acs is given by:

$$\rho_0 = 1.0, \rho_1 = -0.5, \text{ when } \theta_{1,1} = 1.0$$

$$\rho_0 = 1.0, \rho_1 = 0.5, \text{ when } \theta_{1,1} = -1.0$$

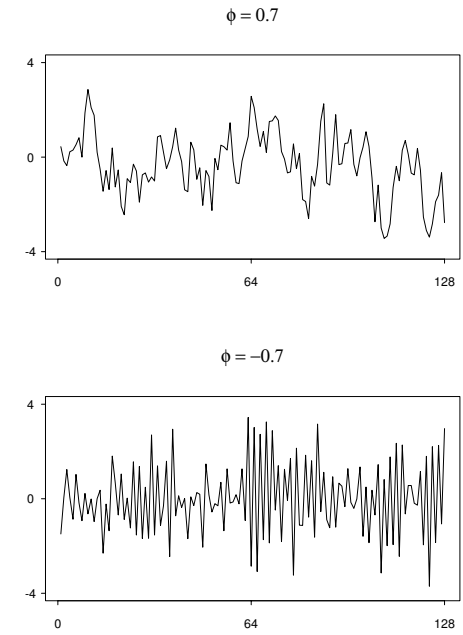


Figure 12: Realizations of size 128 of two first-order Gaussian autoregressive processes. The top and bottom plots are for processes with  $\phi = 0.7$  and  $\phi = -0.7$  respectively, and  $\sigma_\epsilon^2 = 1.0$  in both cases. ( $\phi = \phi_{1,1}$ ).

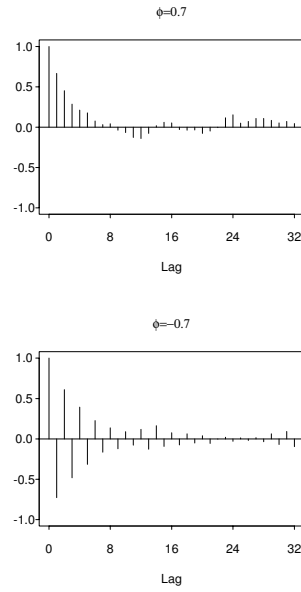


Figure 13: Sample acs for the AR(1) processes shown in Figure 12.

Theoretical acs is given by:

$$\rho_\tau = \phi_{1,1}^{|\tau|}, \quad \tau = 0, \pm 1, \pm 2, \dots$$

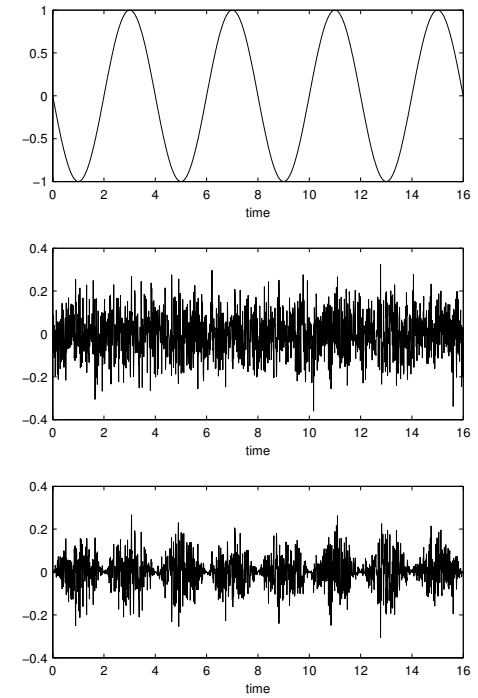


Figure 14: Top plot:  $\cos(2\pi f_0 t + \phi)$ , with  $\phi = \frac{\pi}{2}$ , and  $f_0 = 0.25$ .

Middle plot: simulated random normal process  $\{\epsilon_t\}$ , with  $\sigma_\epsilon = 0.1$ .

Bottom plot: simulated harmonic process,  $X_t = \epsilon_t \cos(2\pi f_0 t + \phi)$ .



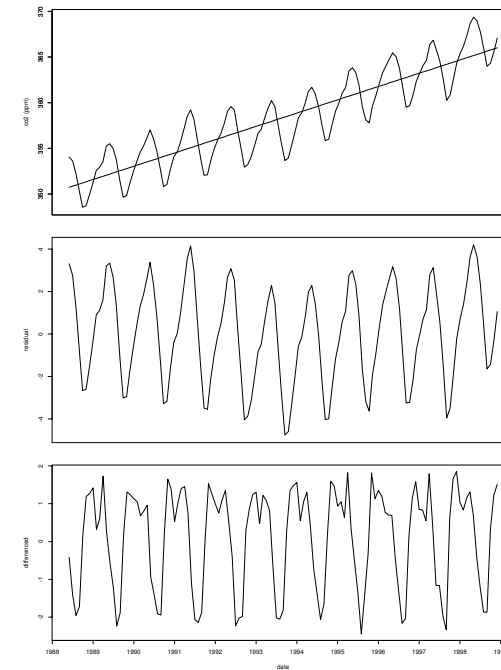
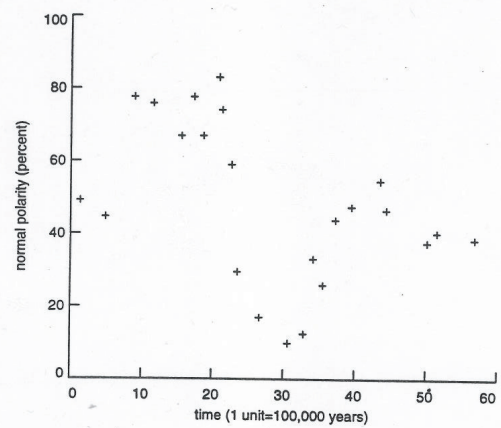


Figure 15: Top plot: Atmospheric CO<sub>2</sub> concentrations (ppmv) derived from in situ air samples collected at Mauna Loa Observatory, Hawaii. The least squares straight line fit is also shown. Source: Keeling & Whorf, Scripps Institution of Oceanography (SIO), University of California.

Middle plot: the residuals from the least squares fit.

Bottom plot: the first differences.

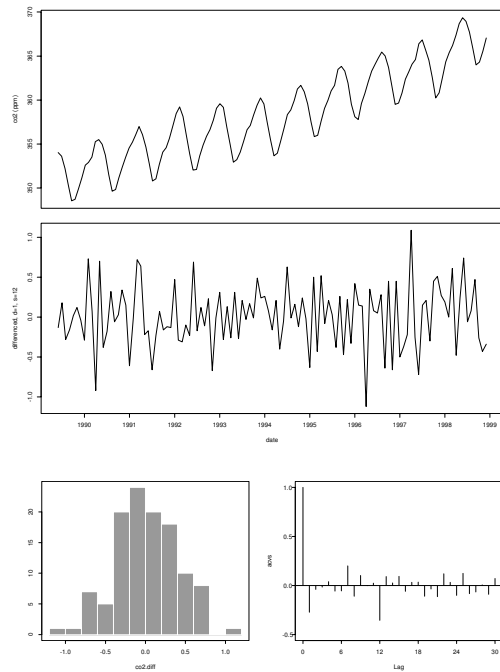


Figure 16: Top plot:  $X_t$ : Atmospheric CO<sub>2</sub> concentrations (ppmv).

Source: Keeling & Whorf, Scripps Institution of Oceanography (SIO), University of California.

Middle plot: first differences, followed by lag 12 differencing.

i.e. applying  $Y_t = (1 - B^s)(1 - B)X_t$  with  $s = 12$ .

Bottom plot (left) histogram of  $Y_t$ .

Bottom plot (right) acvs of  $Y_t$ .

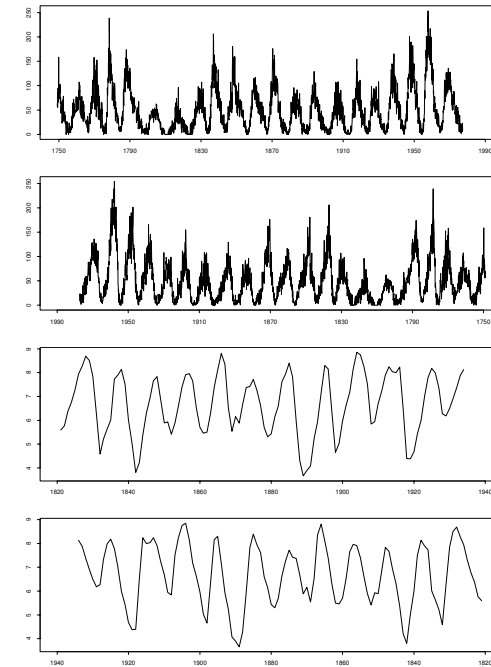


Figure 17: Top two plots: The monthly sunspot numbers (1749 to 1977) in forward and reverse time – note that the values rise more rapidly than they fall.

Bottom two plots: the yearly log Canadian lynx data (1821 to 1934) – again the values rise more rapidly than they fall.

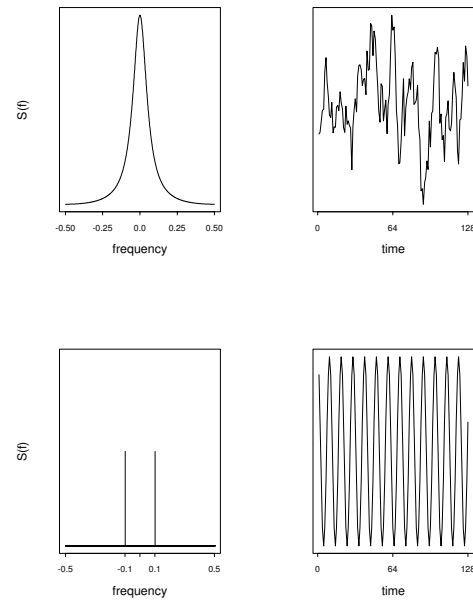


Figure 18: Top row: example of a purely continuous spectrum (left) and one realization of length 128 (right).  
Bottom row: example of a purely discrete spectrum (left) and one realization of length 128 (right).

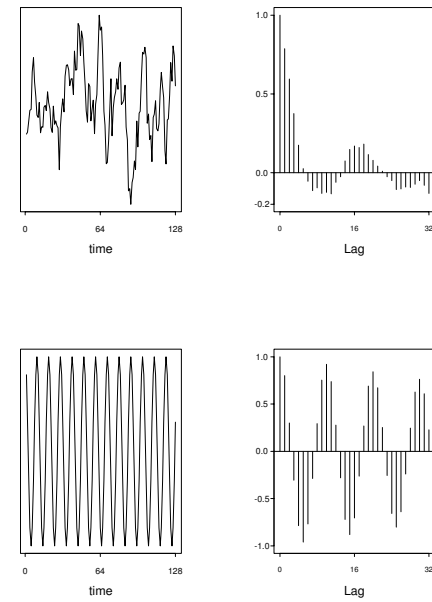


Figure 19: Top row: realization of process with purely continuous spectrum (left) and sample autocorrelation (right).  
Bottom row: realization of process with purely discrete spectrum (left) and sample autocorrelation (right).

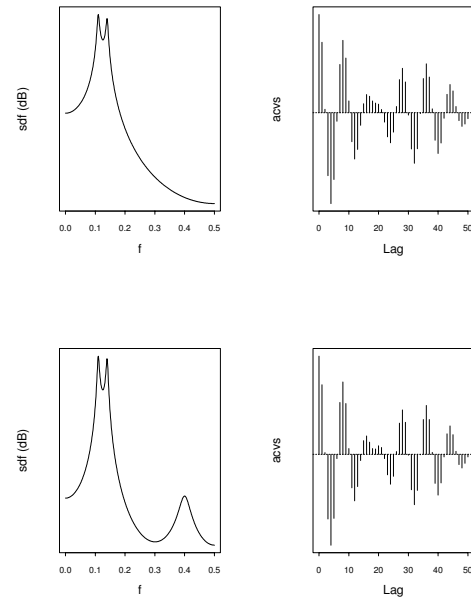


Figure 20: Two spectral density functions (left) and their corresponding autocovariance sequences (right).

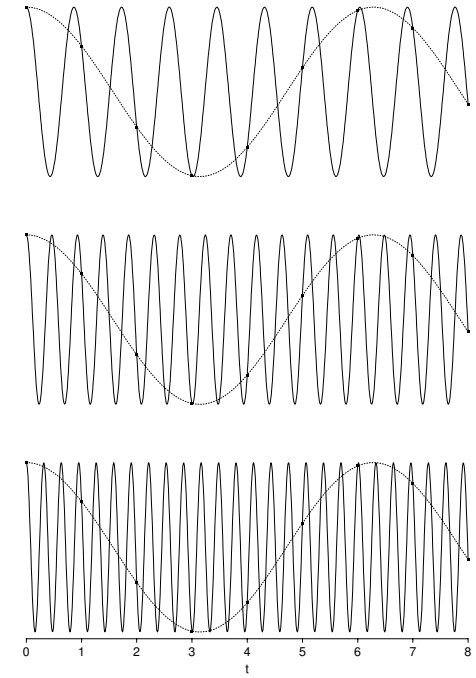


Figure 21: Illustration of the aliasing effect. The dotted curves above show  $\cos(t)$  versus  $t$ . The solid curves show  $\cos([1 + 2k\pi]t)$  versus  $t$  for (from top to bottom)  $k = 1, 2$  and  $3$ . The solid black squares show the common value of all four sinusoids when sampled at  $t = 0, 1, \dots, 8$ .

Fig 21a: The concept of aliasing illustrated for two different sample intervals. In each picture the thin black line is the continuous spectrum, and the thick black line is the resulting spectrum for the discrete process (which is periodic, as shown by its continuation with the thick grey line).

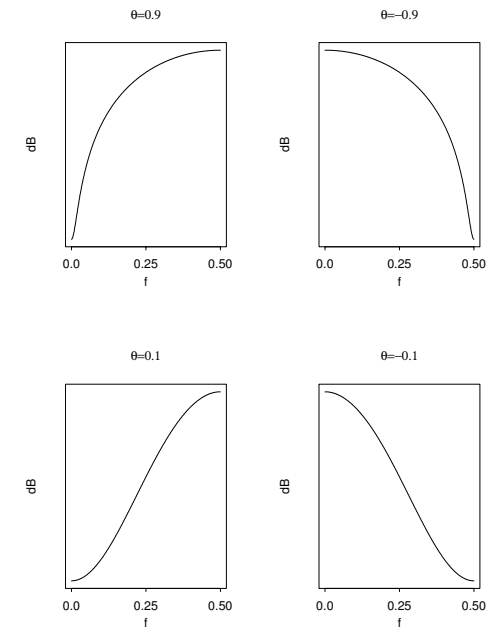
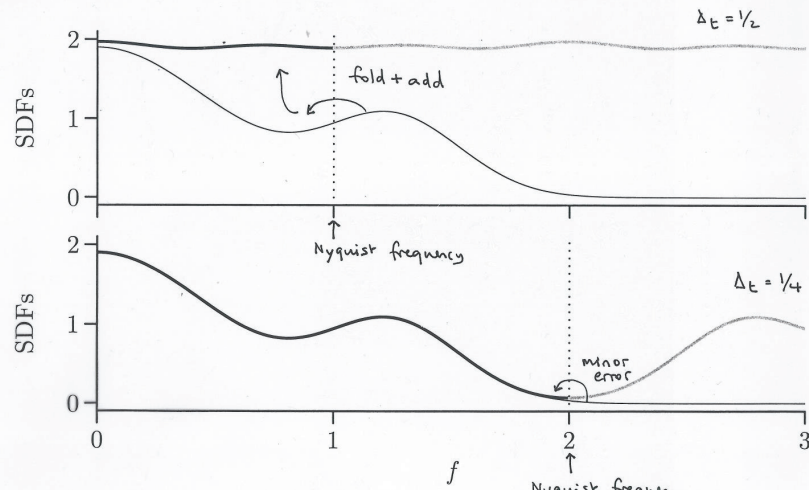


Figure 22: Examples of MA(1) spectra – when  $\theta_{1,1}$  is positive we have a high frequency spectrum and when  $\theta_{1,1}$  is negative we have a low frequency spectrum

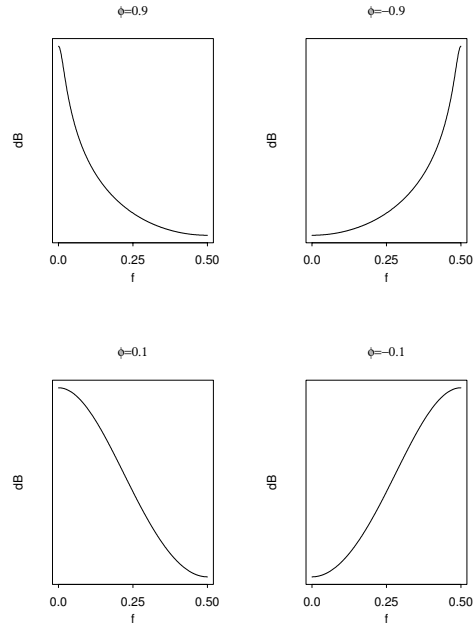


Figure 23: Examples of AR(1) spectra – when  $\phi_{1,1}$  is positive we have a low frequency spectrum and when  $\phi_{1,1}$  is negative we have a high frequency spectrum

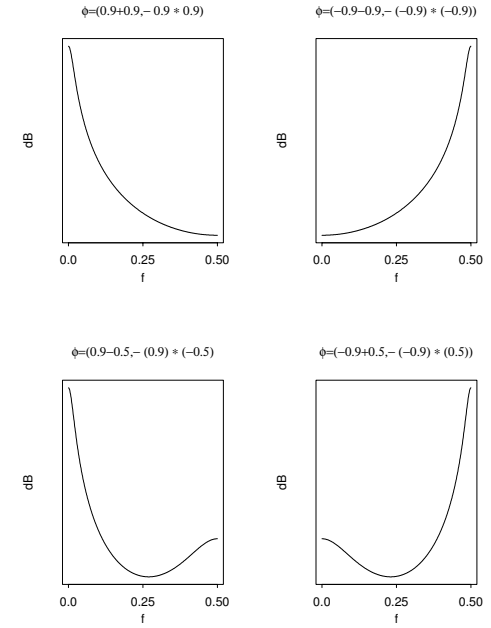


Figure 24: Examples of AR(2) spectra with real characteristic reciprocal roots,  $a = r_1$  and  $b = r_2$ , giving AR parameter values of:  $\phi_{1,2} = r_1 + r_2$  and  $\phi_{2,2} = -r_1 r_2$

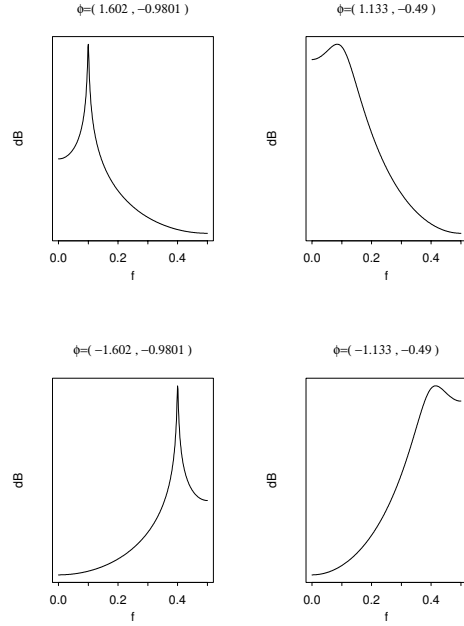


Figure 25: Examples of AR(2) spectra with complex characteristic reciprocal roots,  $re^{\pm i2\pi f}$ , with  $r = 0.99$  for the plots in the left column and  $r = 0.7$  for the plots in the right column, and  $f = 0.1$  for the plots in the first row, and  $f = 0.4$  for the plots in the second row, the AR parameter values (as shown in the titles) can be calculated from  $\phi_{1,2} = 2r \cos(2\pi f)$  and  $\phi_{2,2} = -r^2$

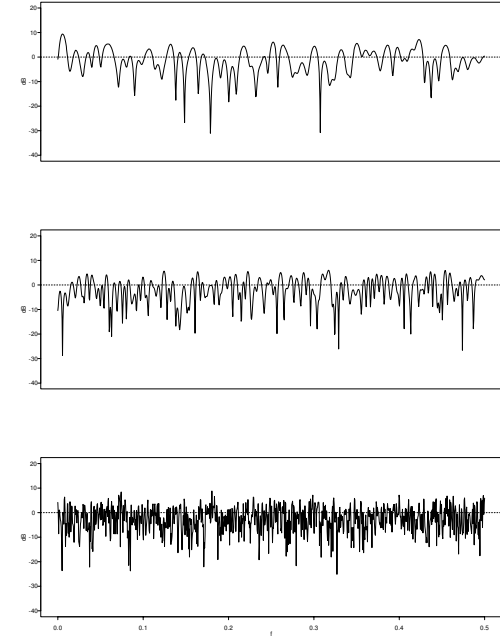


Figure 26: Inconsistency of the periodogram. The plots show the periodogram (on a decibel scale) of a unit variance white noise process of length (from top to bottom)  $N = 128, 256$  and  $1024$ . The horizontal dashed line indicates the true sdf.

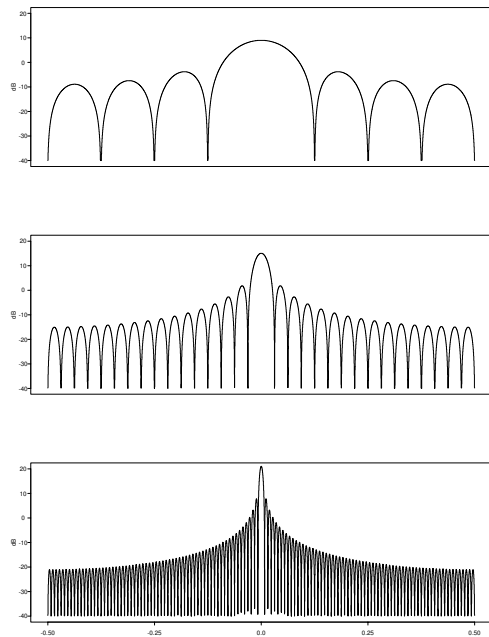


Figure 27: Fejér's kernel for sample sizes  $N = 8, 32$  and  $128$

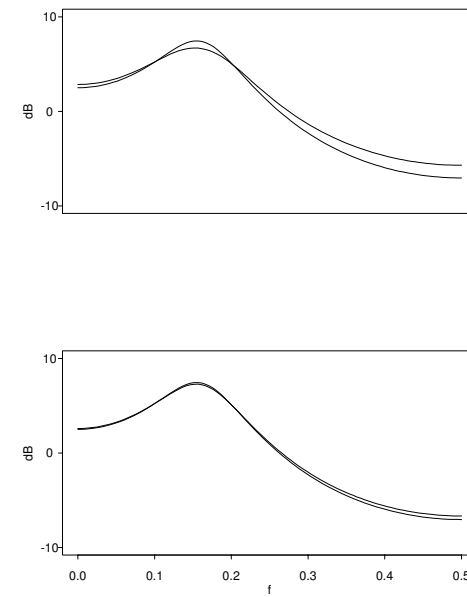


Figure 28: Bias properties of the periodogram for an AR(2) process with low dynamic range. The thick curves are the true sdf  $S(f)$ , while the thin curves are  $E\{\hat{S}^{(p)}(f)\}$  for sample sizes (from top to bottom)  $N = 16$  and  $64$ .



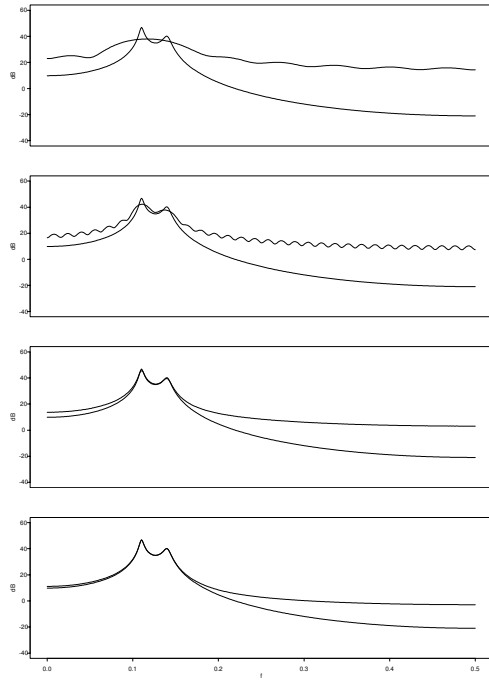


Figure 29: Bias properties of the periodogram for an AR(4) process with high dynamic range. The thick curves are the true sdf  $S(f)$ , while the thin curves are  $E\{\hat{S}^{(p)}(f)\}$  for sample sizes (from top to bottom)  $N = 16, 64, 256$  and  $1024$ .

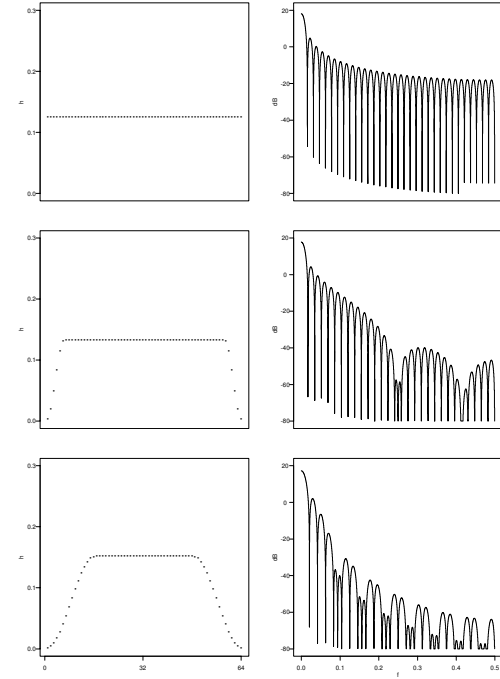


Figure 30: Different data tapers (left column) and associated spectral windows  $\mathcal{H}(f)$  (right column), for  $N = 64$ .

The tapers are a rectangular taper (top), a 20% (middle) and 50% (bottom) split cosine bell taper.

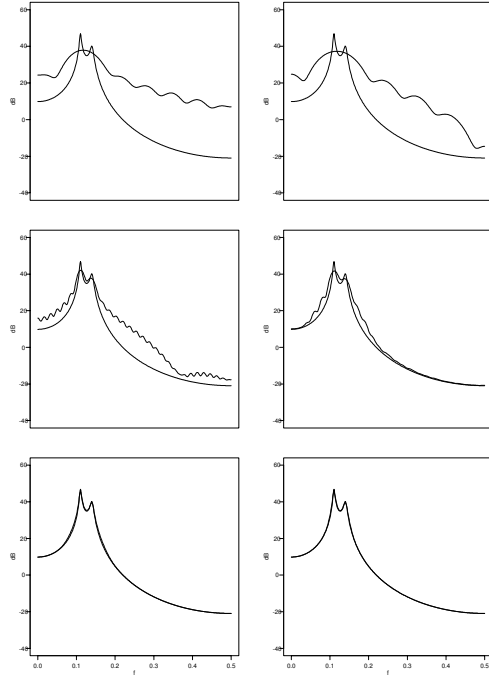


Figure 31: Bias properties of direct spectral estimators for an AR(4) process with high dynamic range, using a 20% (left column) and 50% (right column) split cosine bell taper. The thick curves are the true sdf  $S(f)$ , while the thin curves are  $E\{\hat{S}^{(p)}(f)\}$  for sample sizes (from top to bottom)  $N = 16, 64$  and  $256$ .

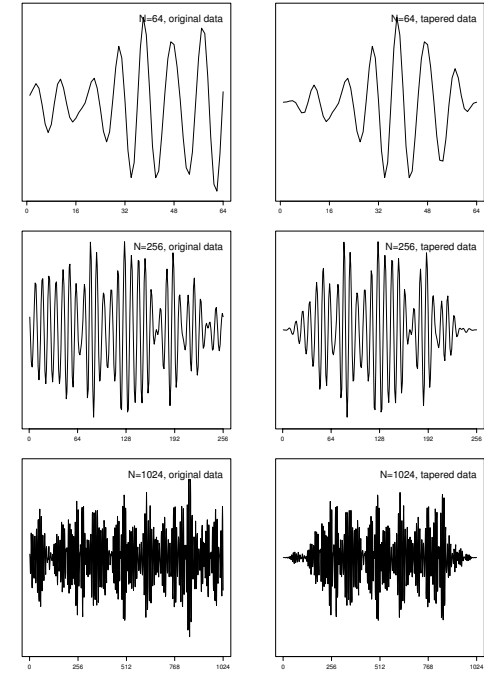


Figure 32: The left column shows simulations from the AR(4) model:

$$X_t = 2.7607X_{t-1} - 3.8106X_{t-2} + 2.6535X_{t-3} - 0.9258X_{t-4} + \epsilon_t$$

For (from top to bottom)  $N = 64, 256$  and  $1024$ .

The right column shows  $\{X_t h_t\}$  where  $\{h_t\}$  is the appropriate length 50% split cosine bell taper.

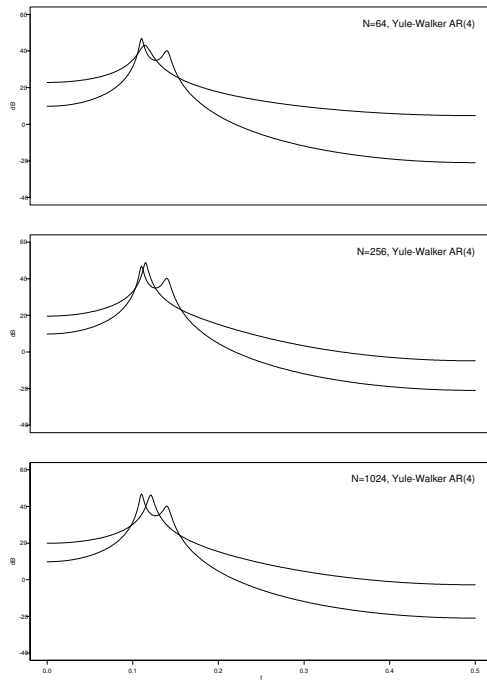


Figure 33: The thick line shows the spectrum of the AR(4) process associated with the Yule-Walker estimates of  $\phi_{1,4}, \dots, \phi_{4,4}$ , for the sequences shown in the left column of Figure 32 (i.e. untapered). The thin line shows the true spectrum.

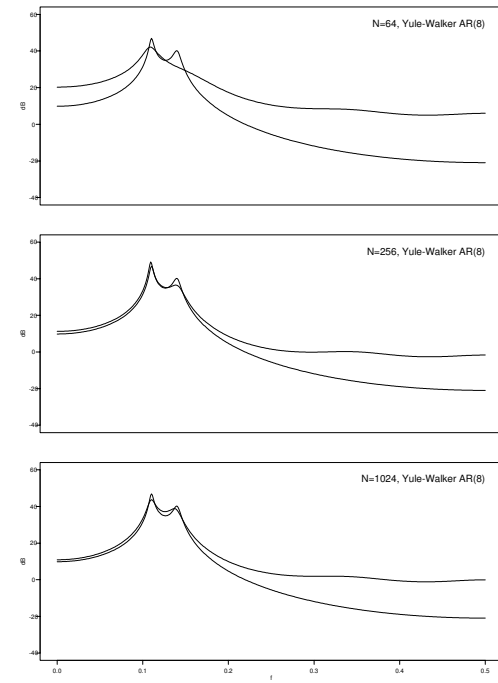


Figure 34: The thick line shows the spectrum of the AR(8) process associated with the Yule-Walker estimates of  $\phi_{1,8}, \dots, \phi_{8,8}$ , for the sequences shown in the left column of Figure 32 (i.e. untapered). The thin line shows the true spectrum.

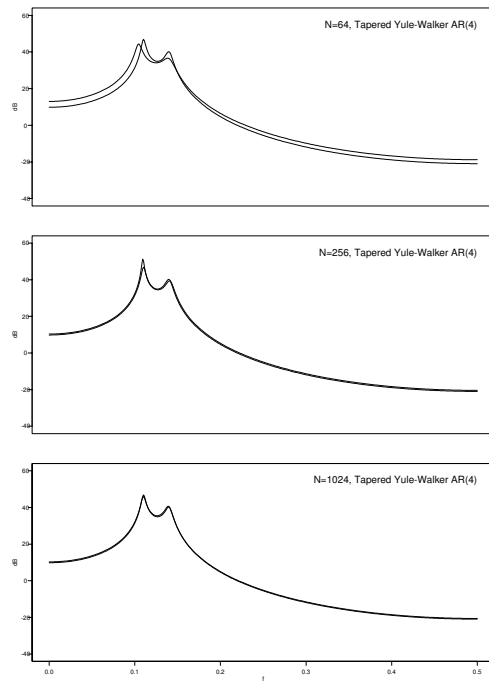


Figure 35: The thick line shows the spectrum of the AR(4) process associated with the Yule-Walker estimates of  $\phi_{1,4}, \dots, \phi_{4,4}$ , for the sequences shown in the right column of Figure 32 (i.e. tapered). The thin line shows the true spectrum.

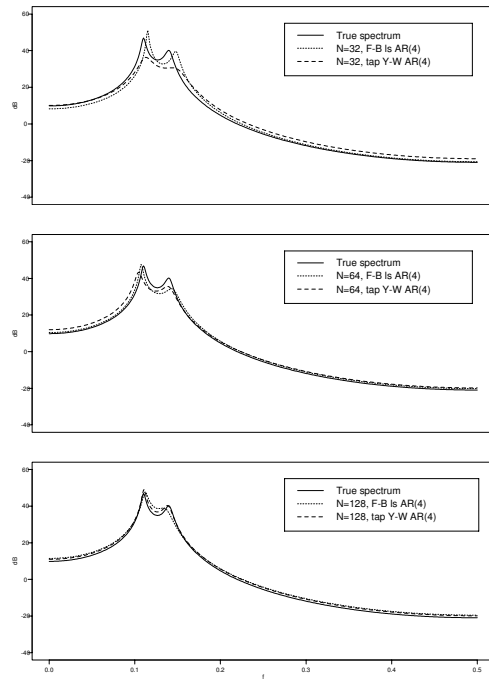


Figure 36: Comparison of F-B least squares and tapered Yule-Walker spectral estimates for the AR(4) process.

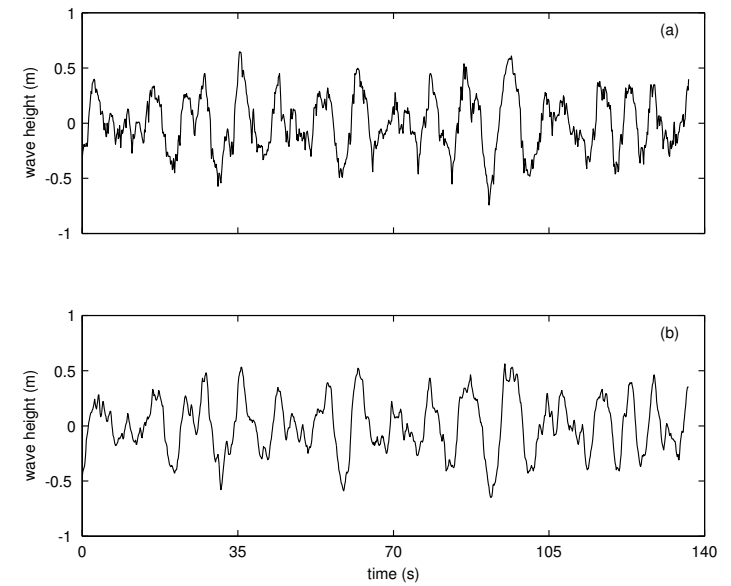


Figure 37: Simultaneous measurements of ocean waves versus time by two instruments of quite different design, (a) an infrared wave gauge, and (b) a wire wave gauge. There are  $N = 1024$  data values in each series and the sample interval is  $\delta_t = 4/30$ s. (These series were derived from data supplied courtesy of Andy Jessup, Applied Physics Lab, University of Washington.)

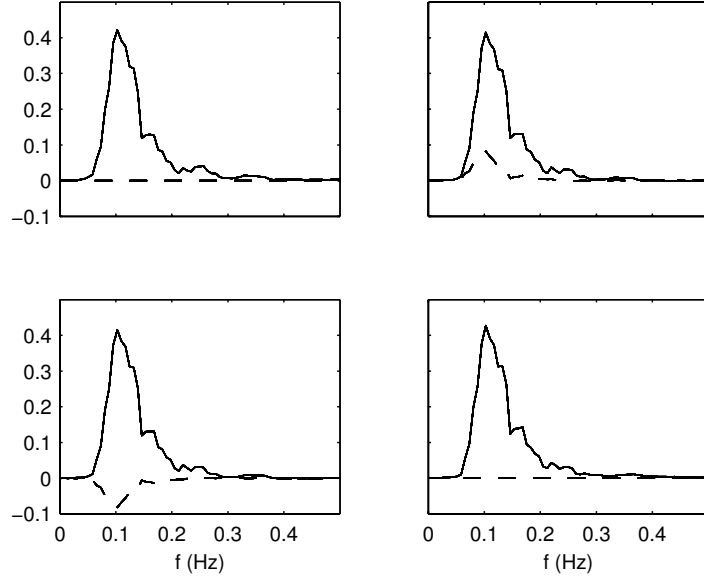


Figure 38: The estimated spectral matrix,  $\hat{\mathbf{S}}(\cdot)$ , for the two ocean wave time series. The real and imaginary parts of  $\hat{S}_{X_l X_m}(\cdot)$ ,  $l, m = 1, 2$ , are shown by solid and dashed lines, respectively.

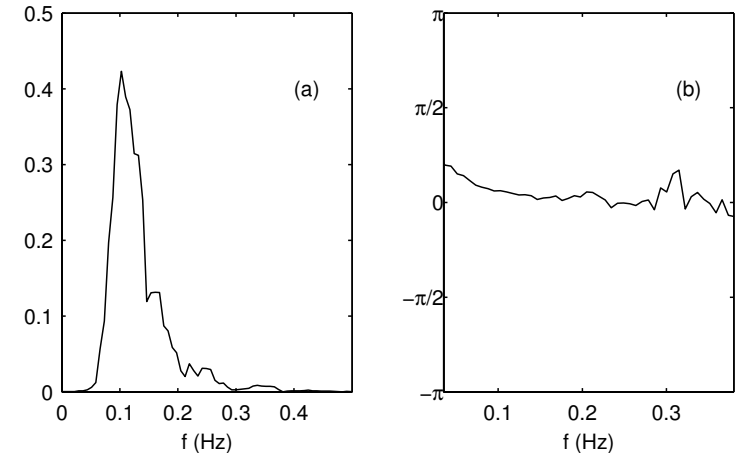


Figure 39: (a) Estimated cross-amplitude spectrum  $|\hat{S}_{X_1 X_2}(\cdot)|$ , in the interval  $[0, 0.5]$  Hz and (b) estimated phase spectrum  $\hat{\theta}_{X_1 X_2}(\cdot)$ , in the interval  $[0.035, 0.38]$  Hz, for the two ocean wave time series .

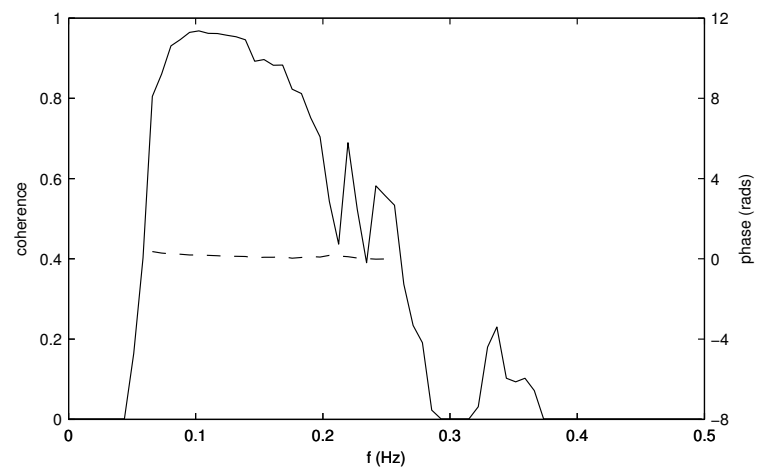


Figure 40: Coherence estimate for the two ocean wave time series. Also shown (dashed line) is the estimated phase  $\hat{\theta}_{X_1 X_2}(f)$  over frequencies for which the estimated ordinary coherence exceeds 0.5.